LANGMUIR Article
Cite This: Langmuir 2017, 33, 14029−14037
pubs.acs.org/Langmuir

Structural Emergence in Particle Dispersions

Andrew Mulderig,[†] Gregory Beaucage,*[,†] Karsten Vogtt,[†] Hanqiu Jiang,[†] Yan Jin,[†] Lisa Clapp,[‡] and Donald C. Henderson[‡]

[†]Department of Materials Science, University of Cincinnati, Cincinnati, Ohio 45221, United States
[‡]Colors Group, Sun Chemical Corporation, Cincinnati, Ohio 45232, United States

Supporting Information

ABSTRACT: Particle dispersions, such as pigment-based inks, comprise weakly bound, milled nanoparticles. The properties of these pigments depend on both their chemical composition and a rather complex structural hierarchy which emerges from these dispersions. The emergence of structure under semidilute conditions is related to the structure of the dilute particles, the particle spacing (mesh size), processing history, and the interaction potential. Kinetic simulations could predict such emergence using these input parameters. In this paper, organic pigments are studied as an example of the importance of emergent structure to predict properties such as brilliance and opacity. Organic pigments are used to impart color to commercial inks, plastics, coatings, and cosmetics. In many cases, dilute pigments are mass fractal structures consisting of aggregated nanoparticles held together by weak van der Waals forces. In water, surfactant is added to create a pigment dispersion (an ink). The final properties of a pigment emerge from a complex interplay between aggregation and dispersion of aggregates as a function of concentration. Samples of the organic pigment yellow 14, PY14, were milled to four primary particle sizes to study the effect on structural emergence. The interaction between surfactant-stabilized PY14 aggregates in an aqueous medium was quantified by the second virial coefficient, A_2, which reflects long-range interactions. The degree of aggregation is associated with short-range attractive interactions between primary particles. In this series of pigments, the degree of aggregation increases dramatically with reduction in primary particle size. Concurrently, the second-order virial coefficient, A_2, increases reflecting stronger long-range repulsive interactions with particle size. Structural emergence can be understood through the percolation concentration and the filler mesh size. A_2 is translated into a repulsive interaction potential for use in dissipative particle dynamics simulations to enable predictive modeling. This description of the interactions between dispersed pigment aggregates allows for a more scientific and predictive approach to understand structural emergence.

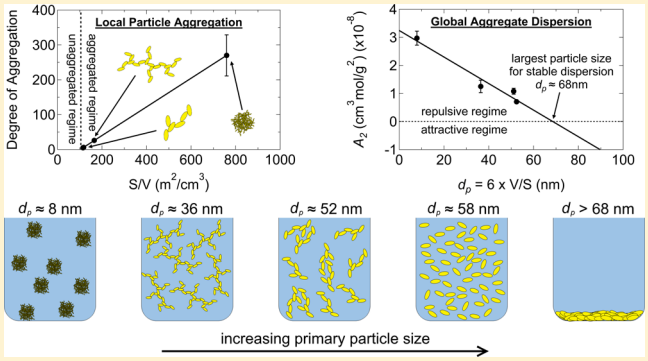

INTRODUCTION

Particle dispersions, such as organic pigments in binders, develop a complex structural hierarchy that is partly responsible for their performance. This hierarchy is typically composed of primary particles (often asymmetric) bonded into ramified aggregates owing to short-range surface potentials. In addition to this structural description, associated with an isolated aggregate in dilute conditions, increase in concentration beyond the overlap concentration into the semidilute regime leads to the formation of an aggregate network governed by a long-range, mean-field potential and excluded volume that can be characterized by an average mesh size. At sizes smaller than the mesh size, the aggregates are structurally comparable to the dilute condition, whereas at larger sizes the structure is obscured and appears uniform. During the processing and drying of organic pigment dispersions, this particulate network structure spontaneously develops. A dried ink or paint retains this emergent aggregate network with pores or binder as the matrix phase. Short-range attractive potentials associated with surface energies are responsible for the aggregation of primary particles, whereas, in many cases, the network structure is governed by a long-range, mean-field potential associated with excluded volume. This can lead to seemingly contradictory observations such as high degrees of primary particle aggregation (indicating poor solvation at a local scale) with good aggregate dispersion (indicating good solvation at large scales). The intent of this paper is to quantify the emergence of this filler network structure in an organic pigment dispersion as well as to understand the structural result of the interplay between short-range and long-range potentials in this emergent structure. In organic pigment dispersions, properties such as brilliance, opacity, and translucency might be related to structural emergence. As an example, aqueous dispersions of pigment yellow 14, PY14, are examined.

Received: August 27, 2017
Revised: November 10, 2017
Published: November 16, 2017

DOI: 10.1021/acs.langmuir.7b03033
Langmuir 2017, 33, 14029−14037

Organic pigments consist of insoluble, crystalline nanoparticles that tend to aggregate into mass fractal structures. Dispersion and aggregation of pigments play a critical role in determining the performance of the pigments in inks, plastics, coatings, and cosmetics.[1−3] Therefore, quantification of the interactions between pigment particles and the matrix phase is of interest to improve dispersion, stability and shelf life. Further, the final appearance of a pigment depends on the interplay between aggregation and dispersion of aggregates as a function of concentration. When an ink or paint dries, the structure of the pigment is locked in and the dispersion of aggregates can then be described by the mean distance between structural features or the mesh size. Although the structure of dried organic pigments may be observed directly via microscope, micrographs only offer qualitative descriptions of dispersion and aggregation of nanoparticles with a small sampling size. Small-angle X-ray scattering (SAXS) and ultra-SAXS (USAXS) have been used to probe the average three-dimensional nanostructure of mass fractal aggregates.[4−6] The same SAXS measurements can be made in solution, in polymer dispersions, as well as in printed inks through the drying cycle. Pigment dispersions are commonly quantified using optical techniques by measuring the absorbance, reflectance, and diffuse scattering of light on dried pigment dispersions.[3,7] However, none of these techniques quantitatively describe the compatibility of a pigment/matrix pair, especially when compared to other compounds, nor do they describe structural emergence with concentration.

Mass fractal aggregates are composed of primary particles that aggregate to form self-similar structures. In some fractal aggregates, such as fumed silica, the primary particles are sintered together to form hard aggregates;[8−10] on the other hand, the primary particles of organic pigments are believed to be bound by weaker van der Waals forces, forming soft aggregates. Thereby, the pigment aggregates may be broken up via mechanical methods, such as milling, and the primary particle size may be reduced. The primary particle size is characterized by the Sauter mean diameter (d_p) that describes the diameter of a sphere with the same surface-to-volume ratio as that of the primary particle.[11] Because small-angle scattering measurements cannot resolve the difference between elongation and polydispersity for aspect ratios less than approximately 2.5, the particles in this category are approximated as spheres.[11] Following size reduction, the pigment primary particles aggregate once more to form mass fractal structures. Several parameters have been introduced to characterize the structure of mass fractal aggregates including a dimensionless aggregate size (R), end-to-end size (R_{eted}), mass fractal dimension (d_f), degree of aggregation (z), minimum path length (p), tortuosity of the minimum path (d_{min}), connective path length (s), and connective dimension (c) (In the Supporting Information Table S2 lists equations used to define these terms). These metrics are related through eq 1.[12−15]

$$R = \frac{R_{eted}}{d_p} = z^{1/d_f} = p^{1/d_{min}} = s^{1/c} \tag{1}$$

These parameters, along with the geometric standard deviation in primary particle size (σ_g), polydispersity index (PDI), and aggregate branch fraction (ϕ_{br}), may be obtained from fits to small-angle scattering data.[11−14,16]

The osmotic pressure, π, in an ideal, dilute colloidal dispersion can be expressed by $\pi/kT = n/V$, in analogy to the ideal gas equation of state, in which k is the Boltzmann constant, T is the absolute temperature, n is the number of dispersed particles, and V is the volume. A virial expansion may be used to quantify deviations from the ideal condition through eq 2 in which R is the ideal gas constant, c_m is the mass concentration of dispersed particles, and M is the molecular weight of the particles.[17−23]

$$\frac{\pi}{RT} = \frac{c_m}{M} + A_2 {c_m}^2 + A_3 {c_m}^3 + \dots \tag{2}$$

Truncation to the second term in the virial expansion is sufficient to quantify binary interactions in the colloidal dispersion through the second virial coefficient, A_2.[17] Positive values of A_2 indicate repulsive interactions between dispersed particles, resulting in a stable suspension. Alternatively, negative values indicate attractive binary interactions, leading to coagulation or flocculation of the colloidal particles and phase separation.[17−22]

The virial approach has not been previously used for pigment dispersions or for fractal particulate dispersions. It has been used to predict phase diagrams for protein and other biological systems[24] as well as for synthetic polymer solutions[25] and monodisperse spherical colloids.[26] Quantification of the mesh size, percolation concentration, and the particle size dependence of A_2 using the virial approach, discussed below, are absent from the literature.

The unified scattering function, eq 3, may be used to characterize small-angle scattering from arbitrary mass fractal structures across multiple hierarchical structural levels by coupling Guinier's law and power law at each structural level "i".[1,4,5,27]

$$I(q) = \sum_{i=1}^{n} \{G_i\, e^{-q^2 {R_{g,i}}^2/3} + e^{-q^2 {R_{g,i+1}}^2/3} B_i q_i^{*-P_i}\}$$
$$q_i^* = \frac{q}{\left(\mathrm{erf}\left(\frac{kqR_{g,i}}{\sqrt{6}}\right)\right)^3} \tag{3}$$

"k" has a value of 1.06 for mass fractal levels and 1 for dense structural levels. The momentum transfer vector, q, is defined in terms of the X-ray wavelength, λ, and scattering angle, θ, through eq 4.[28]

$$q = \frac{4\pi}{\lambda} \sin\left(\frac{\theta}{2}\right) \tag{4}$$

Because the scattered intensity is directly proportional to the volume fraction of scatterers, one would expect $I(q,\phi)/\phi$ to remain constant for all samples in a concentration series. However, the normalized scattering intensity is diminished in the low-q regime because of structural screening, which is associated with the emergence of a random pigment network. For non-agglomerated aggregates, $I(q,\phi)$ remains constant at the lowest-q below the mesh size.[18,19,23,29] By measuring the small-angle scattering from otherwise similar pigment dispersions at different concentrations, the screening parameter, ν, may be determined by eq 5.[18,23,30]

$$\frac{I(q,\phi)}{\phi} = \left(\frac{\phi_0}{I(q,\phi_0)} + \phi\nu\right)^{-1} \tag{5}$$

in which $\nu = 2A_2 N_A \frac{{\rho_m}^2}{(\Delta\rho)^2}$.

DOI: 10.1021/acs.langmuir.7b03033
Langmuir 2017, 33, 14029−14037

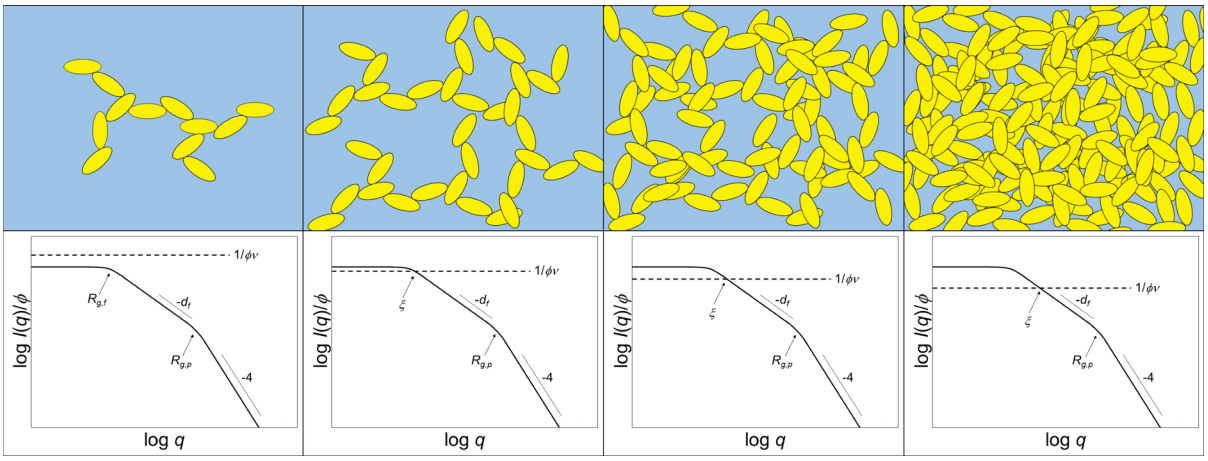

Figure 1. The top row shows cartoon depictions of the dispersed particle aggregates. The bottom row shows the corresponding one-dimensional small-angle scattering data for the above cartoons. In the dilute condition, structural features can be observed at all length scales (left). As the concentration increases (going from left to right), the species of interest begin to overlap. Larger features become obscured owing to the screening for $I(q)/\phi$ larger than $1/\phi\nu$ in the bottom graphs. The dilute scattering curve (solid line in the left plot) is depressed in the low-q regime following the horizontal dashed line at higher concentrations to the right. Instead of the aggregate size, the largest observable structural feature is now the emergent mesh size, ξ. The mesh size quantifies the mean distance between structural features at concentrations above the overlap concentration in the top sketches. At higher concentrations, the mesh size continues to decrease ($\xi = 2\pi/q_m$), and the information about larger structural features (at lower q) is lost in scattering.

Equation 5 is a variant of the random-phase approximation (RPA) for a binary mixture, and ν reflects a mean field, acting on the pigment aggregates.[30] $I(q,\phi)$ denotes the intensity of the scattered X-rays as a function of momentum transfer vector, q, and the pigment volume fraction, ϕ. N_A is Avagadro's number, ρ_m is the mass density of the pigment, and $\Delta\rho$ is the scattering length density contrast between the pigment and the aqueous medium. ϕ_0 is the volume fraction of scatterers in the dilute condition below the pigment overlap concentration. In SAXS measurements, only the surfactant-stabilized pigment particles are observed.

Figure 1 depicts structural screening for colloidal dispersions of fractal aggregates. In dilute conditions, shown on the left in Figure 1, all structural features of the aggregate can be observed, and the magnitude of $\phi\nu$ is relatively low compared to $\phi/I(q)$ in eq 5.[18,23] As the concentration increases, larger structural features, such as aggregate size, are screened owing to the overlap of the aggregates. At these length scales, a characteristic mesh size, ξ, emerges that describes the size of the openings in the network. The mesh size is the average separation between neighboring structural features as has been demonstrated in transmission electron micrographs in a previous publication.[23] For a concentration series of otherwise similar dispersions, ν is a constant value describing the thermodynamic stability of the colloidal dispersion. Positive values of ν indicate repulsive interactions, leading to a stable suspension, whereas negative values indicate attractive interactions, resulting in an unstable suspension.[18−23] The value of ν can be tuned by the use of surfactants, flocculants, solvent type, or other agents affecting particle−particle interactions.[21,31−33] In the absence of entropic effects and excluded volume, the boundary between stable and unstable regimes for an ideal dispersion occurs at $\nu = 0$. In many systems, however, the boundary value has negative contributions from the excluded volume.[18,19,23] By fitting the scattering data using eqs 3 and 5 for sample sets of increasing pigment concentration, it is possible to measure the second-order virial coefficient, A_2.

For repulsive binary interactions (indicating stable dispersions), the second virial coefficient may be determined via small-angle scattering measurements. Furthermore, the value of A_2 may be employed in the predictive modeling of aggregate dispersions through the calculation of the binary interaction potential, $U(r)$. The second virial coefficient is related to $U(r)$ between dispersed aggregates through eq 6 in which k_B is the Boltzmann constant, M is the molecular weight, N_A is Avogadro's number, and σ is the average end-to-end size of the aggregate.

$$B_2 = \frac{A_2 M^2}{N_A} = 2\pi \int_0^{\sigma} r^2 \left[1 - \exp\left(-\frac{U(r)}{k_B T}\right)\right] dr \tag{6}$$

If aggregates do not interpenetrate, σ is calculated by $\sigma = R_{eted} = d_p p^{1/d_{min}}$. Using a predictive modeling technique such as dissipative particle dynamics (DPD), it becomes possible to translate the values of A_2 into parameters describing the binary repulsive interactions, which may be employed in simulations of dispersed filler aggregates. Specifically, the repulsive force in DPD simulations is often given by eq 7, where "A" is the magnitude of the repulsive binary interactions and σ is the cutoff distance of the repulsive interactions.[34−37] A is proportional to the Hamaker constant.[38]

$$\frac{U(r)}{kT} = \frac{A}{2}\left[1 - \left(\frac{r}{\sigma}\right)\right]^2 \tag{7}$$

Through eqs 6 and 7, the second virial coefficient can be translated into the magnitude of repulsive interactions in DPD simulations, A. In this way, the emergent structure may be simulated. Quantification of interactions between the dispersed pigment aggregates allows for a more complete understanding of suitable conditions to prepare dispersions of organic pigments and may enable optimization of high-performance organic pigments.

DOI: 10.1021/acs.langmuir.7b03033
Langmuir 2017, 33, 14029−14037

EXPERIMENTAL SECTION

Aqueous colloidal dispersions of PY14 were obtained from Sun Chemical Corporation and used as received. The PY14 particles were milled to four different primary particle sizes (A, B, C, and D). A concentration series for each particle size was prepared by dispersing PY14 in water using the Triton X-100 ($C_{14}H_{22}O(C_2H_4O)_n$) surfactant to stabilize the dispersions. The Triton X-100 concentration was about 1 mg/mL (1.6 mM or about seven times the critical micelle concentration) for all samples.[39] At this surfactant concentration, the pigment surface coverage is independent of the surfactant concentration.[39] The USAXS and SAXS measurements were performed on the beamline 9-ID-C operated by the X-ray Science Division at the Advanced Photon Source (APS) at Argonne National Laboratory.[40,41] A momentum transfer vector, q, of 0.0001 Å^{-1} ≤ q ≤ 0.8 Å^{-1} was accessible by this combination of instruments. The Indra and Irena packages for Igor Pro were employed to reduce, desmear, and merge the data sets.[27] The SAXS and USAXS data sets were merged using the absolute scale of the USAXS measurements. Background scattering from the aqueous medium was subtracted prior to data stitching.

RESULTS AND DISCUSSION

Figure 2 shows the combined reduced USAXS and SAXS data, $I(q)/\phi$, for a concentration series of dispersed PY14 aggregates milled to the smallest primary particle size (sample series A). The USAXS data for the sample series B, C, and D are shown in Figures S2−S4, respectively. The SAXS data for the dilute PY14 samples are given in Figure S5.

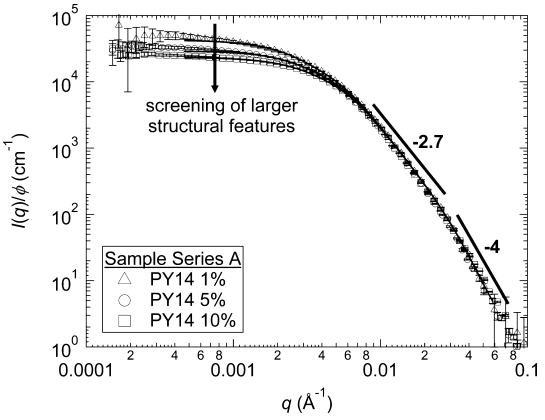

Figure 2. Reduced small-angle scattering data, $I(q)/\phi$, from aqueous dispersions of the smallest PY14 primary particles, series A, normalized by pigment volume fraction. Samples of 1, 5, and 10% (by weight) were measured in sample series A. In the high-q regime, screening is not observed, and the curves overlap. The large-scale structure at low-q is increasingly screened at higher concentrations. The extent of structural screening is proportional to the concentration and is used to determine A_2 through eq 5.

The small-angle scattering data for each sample were fit using eqs 3 and 5 to determine the mass fractal aggregate structure and to determine the extent of structural screening, respectively. The power-law slope of −4 in the high-q regime indicates dense primary particles with smooth surfaces. Within each concentration series, the mass fractal structure is consistent. Among the series, A, B, C, and D, the nanostructure varies with the primary particle size. In sample series A, ramified mass fractal aggregates of fractal dimension d_f = 2.7 were observed. On the other hand, the aggregates of larger primary particles displayed lower fractal dimension of roughly d_f = 1.4, suggesting the presence of more open structures as indicated by the connectivity dimension that drops from 1.66 for series A to about 1 for the other series. "c" of 1 indicates an unbranched or "linear" aggregate. Samples in the concentration series B, C, and D display a primary particle size about one order of magnitude larger than those in sample series A. It is expected that smaller primary particles will lead to higher degrees of branching because of the larger specific surface area and greater electrostatic interactions per primary particle.[15] In each sample series, screening of larger structural features was observed for semidilute dispersions, and the extent of structural screening was compared to dilute samples to quantify the screening parameter, ν.

Because the scattered intensity is proportional to volume fraction, $I(q)$ was normalized by the pigment volume fraction to quantify the extent of screening as a function of pigment concentration. In the absence of screening, the scattering curves shown in Figure 2 would superimpose across the entire q-range. Although the normalized small-angle scattering superimposes at high-q across the concentration series, screening of the larger structural features leads to a diminution in the reduced scattered intensity at low-q for higher concentrations. The overlap concentration or percolation threshold is calculated by equating the Guinier prefactor for the PY14 fractal aggregates to the magnitude of screening through eq 8

$$\frac{1}{\phi_{\text{overlap}}\upsilon} = G_2 \tag{8}$$

This limits the pigment mesh size to sizes smaller than the aggregate size related to the percolation threshold. At high concentrations, the mesh size is limited by the primary particle size. The radius of gyration for the first structural level, $R_{g,1}$, gives an estimate of the primary particle size. The high-concentration limit is calculated by substituting G_1 for G_2 in eq

Table 1. Fitting Parameters for Unified Scattering Function Fit to USAXS Data for Dilute Dispersions of PY14

dilute PY14 sample	A	B	C	D
G_1 (×10^{3}cm^{-1})	0.105 ± 0.03	100 ± 1	330 ± 1	300 ± 1
$R_{g,1}$ (Å)	68 ± 3	450 ± 1	590 ± 1	600 ± 1
B_1 (×10^{-6} cm^{-1} Å^{-4})	36 ± 6	54 ± 1	45 ± 1	38 ± 1
P_1	4	4	4	4
G_2 (×10^{3}cm^{-1})	28 ± 1	2700 ± 1	1600 ± 1	2000 ± 1
$R_{g,2}$ (Å)	550 ± 5	3900 ± 3	3500 ± 2	2700 ± 4
B_2 (×10^{-3} cm^{-1} Å$^{-P_2}$)	6.2 ± 0.7	40000 ± 200	38000 ± 200	52000 ± 1000
P_2	2.70 ± 0.02	1.41 ± 0.01	1.40 ± 0.01	1.44 ± 0.01
ν (×10^{-5} cm)	32 ± 1	3.2 ± 0.3	2.2 ± 0.1	1.7 ± 0.1
ϕ_{overlap}	0.096 ± 0.004	0.012 ± 0.001	0.029 ± 0.001	0.031 ± 0.001

DOI: 10.1021/acs.langmuir.7b03033
Langmuir 2017, 33, 14029−14037

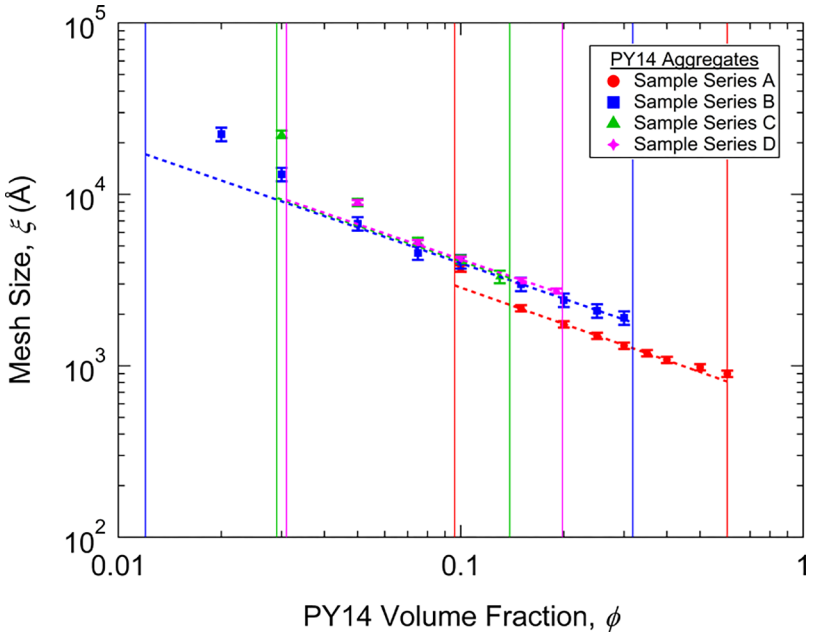

Figure 3. log–log plot of mesh size vs PY14 volume fraction. Mesh size is of interest because it may correlate with spectral properties such as brilliance and opacity. The overlap concentration and the high-concentration limit of mesh size at the primary particle size are calculated via eq 8 using G_2 and G_1, respectively. They are indicated by vertical lines. The mesh size cannot decrease to the primary particle size, but only pigment volume fractions up to about 0.6 are achievable in the case of a dried ink or coating because of packing constraints. The dotted lines are the calculated screening length from eq 8 between these limits. Deviation from this power law of mesh size with PY14 volume fraction is observed when $1/\phi\nu$ intersects a Guinier regime of the scattering curve at sizes associated with the aggregates and primary particles.

8. Table 1 shows the fitting parameters for the unified scattering function for the dilute (1 wt %) suspensions of each series.

The radius of gyration of the aggregates, $R_{g,2}$, can be measured for the dilute samples but is obscured at higher concentrations because of screening. It is important to note, however, that the structural screening of larger structural features does not correspond to changes in the aggregate structure at these length scales.[12−15] The point of intersection of $1/\phi\nu$ with $I(q,\phi)/\phi$ for the dilute sample yields q_m corresponding to the emergent mesh size via $\xi = 2\pi/q_m$.[23,42] Mesh size is an important emergent property in inks and paints because it may correlate with spectral properties such as brilliance and opacity. At higher concentrations (such as those observed during pigment drying), the extent of structural screening intersects a power-law regime of the scattering curve. By equating the extent of structural screening to the power-law scaling, one obtains $\frac{1}{\phi\nu} = B_2 q_m^{-d_f}$ in which B_2 and d_f describe the fractal power-law regime observed in USAXS measurements. Substituting the mesh size for $2\pi/q_m$, a power-law relationship for the mesh size in concentration is obtained

$$\xi = 2\pi\left(\frac{1}{B_2\phi\nu}\right)^{1/d_f} \tag{9}$$

The power-law trend in ξ versus ϕ enables prediction of the emergent mesh size as the PY14 concentration increases, for example, during drying of aqueous inks.

Figure 3 illustrates the scaling of mesh size with concentration. The dotted lines are calculated by eq 9 assuming that the intersection of $1/\phi\nu$ and the scattering curve occur in the power-law regime. Deviation from the $-1/d_f$ scaling of eq 9 is observed when $1/\phi\nu$ intersects the scattering curve in the Guinier regime at low-q corresponding to the aggregate (percolation threshold) and at high-q to the primary particles (high concentration).

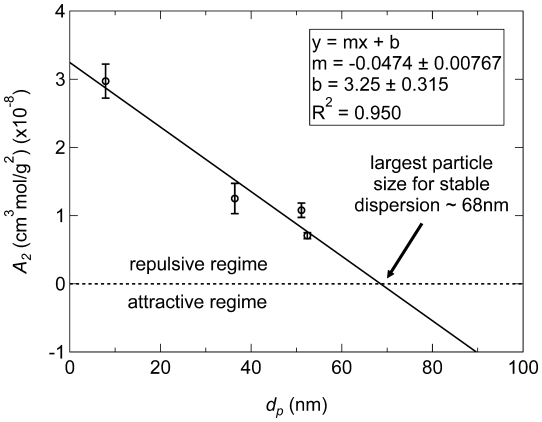

Figure 4. Plot of A_2 vs d_p showing a close to linear dependence in particle size. The intersection of this trend (solid line) with the excluded volume contribution to A_2 (dashed line) indicates the particle size above which aqueous PY14 aggregate dispersions would not be stable. The positive $d_p = 0$, y-intercept at about 3.2×10^{-7} cm^3 mol/g^2, indicates favorable interfacial interactions in this dispersion because of the presence of a surfactant. A_2 reflects long-range interactions.

Values of the second-order virial coefficient, A_2, are calculated using eq 5 for each concentration series of variable primary particle size, d_p. Since both the PY14 aggregates and the Triton X-100 surfactant have neutral charge, the inks are primarily stabilized by steric interactions of the surfactant-coated PY14 aggregates. A decreasing trend in A_2 and, therefore, decreasing stability of the PY14 dispersions, is identified for increasing primary particle size in the PY14 aggregates. A plot of A_2 versus PY14 primary particle size is given in Figure 4. The vertical intercept of A_2 versus d_p, shown

DOI: 10.1021/acs.langmuir.7b03033
Langmuir 2017, 33, 14029−14037

Table 2. Parameters Describing Primary Particles, Fractal Structure, and the Second-Order Virial Coefficient, A_2, Derived from the Unified Scattering Function and eq 5 for PY14 Samples of Different Primary Particle Sizes[a]

PY14 sample set	A	B	C	D
d_p (nm)	8 ± 1	36.4 ± 0.1	51.1 ± 0.1	52.4 ± 0.1
σ_g	1.43 ± 0.01	1.59 ± 0.01	1.55 ± 0.01	1.6 ± 0.01
PDI	4.7 ± 0.2	13.0 ± 0.1	10.2 ± 0.1	10.0 ± 1.0
z	270 ± 90	26 ± 1	6 ± 1	5 ± 1
p	29 ± 6	21 ± 4	6 ± 1	5 ± 1
s	32 ± 7	12 ± 2	4 ± 1	3 ± 1
d_{min}	1.61 ± 0.20	1.33 ± 0.07	1.40 ± 0.04	1.44 ± 0.06
c	1.66 ± 0.2	1.06 ± 0.06	1.00 ± 0.03	1.00 ± 0.04
d_f	2.67 ± 0.02	1.41 ± 0.01	1.40 ± 0.01	1.44 ± 0.01
ϕ_{br}, %	89 ± 2	20 ± 20	0 ± 5	0 ± 6
A_2 ($\times 10^{-9}$ g^{-2} cm^3 mol)	30 ± 1	13 ± 1	10.8 ± 0.5	7.1 ± 0.2
DPD "*A*"	12.3 ± 2.0	1.46 ± 0.01	5.02 ± 0.03	2.36 ± 0.01

[a]Calculated values of the DPD repulsive magnitude, *A*, are also given. Parameters were calculated according to the equations listed in Table S2.

in Figure 4, reflects the dispersive interaction for particles composed completely of surface because $S/V = 6/d_p$. This $d_p = 0$ intercept indicates the interfacial repulsion in the absence of particle size effects in aqueous pigment dispersions of PY14 using the Triton X-100 surfactant. The value is expected to vary depending on the chosen dispersing medium and surfactant. Sinced the vertical intercept is positive, dispersions of smaller primary particles are expected to be more stable. Competition between surface repulsive forces favoring dispersion by Brownian motion and coagulation forces associated with the particle volume and mass may lead to a reduction in A_2 with increasing primary particle size. Since the inks measured in this experiment were stable (having positive values of A_2), sedimentation was not observed in the time scale of the scattering experiment. Larger primary particles are associated with lower specific surface area and less particle interaction. The decreased magnitude of repulsive binary interactions between dispersed particles indicates a less stable colloidal suspension. The slope of the trend in A_2 with primary particle size indicates the sensitivity of dispersion stability to particle size for PY14 aggregates. The size-dependent stability of the suspended particles can be tuned through the use of different surfactants and dispersing media.

The dashed line at $A_2 = 0$ shows the boundary between repulsive (stable) and attractive (unstable) regimes for a colloidal dispersion. This is a conservative estimate for the boundary value of A_2 between attractive and repulsive regimes because real dispersions will have contributions to A_2 from the excluded volume of the primary particles, $V_{ex} = 2\pi N_A d_p^3/3$. The van der Waals contributions to the boundary value of A_2 can be quantified via USAXS measurements on a concentration series of pigment dispersions at several different temperatures, but this is beyond the scope of the current work.

The point at which the trend line in A_2 versus d_p crosses $A_2 = 0$ indicates the maximum size of primary particles that can form a stable aqueous dispersion using the Triton X-100 surfactant, roughly 68 nm for the PY14 dispersions assuming no excluded volume. Aggregates of PY14, with primary particles larger than this size, will tend to coagulate. Because PY14 has a density of 1.45 g/cm^3, the pigment aggregates would sediment out of the unstable dispersion; if the particles had a lower density than the dispersing medium, the particles would froth. Because dispersions having higher values of A_2 are more thermodynamically stable, it is expected that PY14 dispersions of smaller primary particles will have longer shelf life. Values of A_2 for PY14 aggregates from the four series are shown in Table 2.

The topology of dispersed PY14 aggregates was characterized using literature methods for mass fractal aggregates in each sample series and is summarized in Table 2.[12−15] Scattering from dilute samples in each series was analyzed because the large-scale structure of the fractal aggregates is screened at higher concentrations following eq 5. Larger primary particles were more polydisperse (σ_g and *PDI*) and tended to form linear aggregates ($c \approx 1$) with polydisperse primary particles and lower degrees of aggregation ($z \approx 5$). Smaller primary particles, on the other hand, had less polydisperse primary particles and tended to form highly ramified mass fractal aggregates ($c > 1$). The branch fraction in fractal aggregates is calculated by $\phi_{br} = (z - p)/z$.[11,12,15,42] It can be inferred from the high values of d_{min}, c, d_f, and ϕ_{br} that series "A" results in hyperbranched aggregates with a high fraction of internal segments, segments with both ends connected to branch points. Comparison of G_2 and G_1 suggests that the aggregates of smaller primary particles show a higher degree of aggregation, given by $z = 1 + G_2/G_1$.[23,42,43]

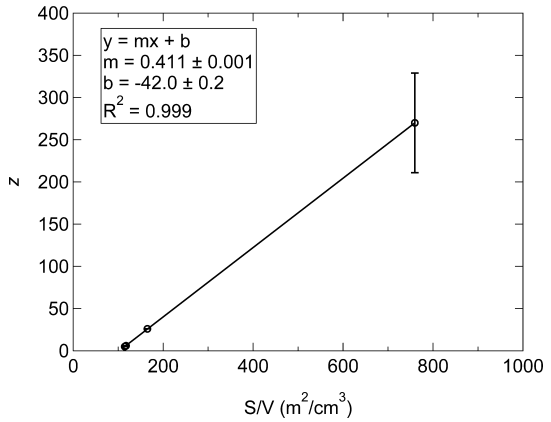

Figure 5. Degree of aggregation, z, vs specific surface area, S/V for sample series A–D. $z = 1$ represents unaggregated primary particles; this is projected to occur at $d_p = 57.3$ nm or $S/V = 105$ m^2/cm^3. The linear fit in Figure 5 follows $z = 2465/d_p - 42$. The high goodness of fit to the four data points suggests a strong dependence of degree of aggregation on specific surface area. "z" reflects the strength of short-range interactions between primary particles.

DOI: 10.1021/acs.langmuir.7b03033
Langmuir 2017, 33, 14029−14037

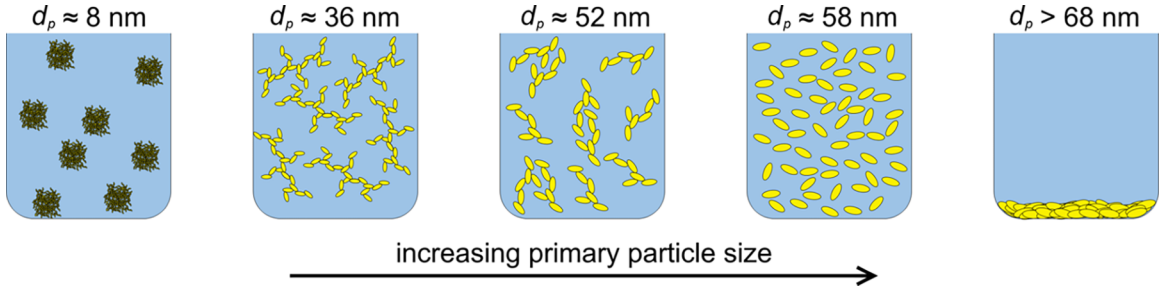

Figure 6. Schematic illustrating the competition between local primary particle aggregation and long-range aggregate dispersion for PY14 aggregates of increasing primary particle size. Smaller particles, such as those in sample series A, form aggregates of high z and are the most well-dispersed. Samples in series B, C, and D are dispersed yet form aggregates of lower z. As A_2 decreases, local clustering of aggregates becomes more prominent. At primary particle sizes greater than about 58 nm, PY14 primary particles are predicted to not aggregate. At $d_p > 68$ nm, unaggregated primary particles are predicted to settle out of the dispersion.

Figure 5 plots the degree of aggregation, z, against the specific surface area of the PY14 aggregates. The first two points in S/V overlap. Following a linear regression, z is observed to be close to proportional to the specific surface area. The degree of aggregation can be likened to a measure of short-range interactions between the nanoparticles. Extrapolating the trend in Figure 5 predicts unaggregated primary particles ($z = 1$) to have a specific surface area of about 105 m^2/cm^3 ($d_p = 57.3$ nm). Given the trend in A_2 versus primary particle size shown in Figure 4, an aqueous dispersion of such unaggregated PY14 nanoparticles with the Triton X-100 surfactant is expected to be stable. It is interesting to note that Figure 4 shows that particles larger than 68 nm should fall out of solution owing to the reduction in long-range repulsive interactions, whereas Figure 5 shows that particles larger than about 58 nm do not aggregate owing to a reduction in the short-range attractive interactions related to a reduced surface-to-volume ratio. Primary particle size of around 60 nm is the cutoff for both long-range and short-range interactions. Upon closer inspection of Figures 4 and 5, trends in both degree of aggregation and dispersibility as functions of primary particle size are obtained. The competition between local primary particle aggregation and long-range aggregate dispersion with variation in primary particle size is illustrated in Figure 6.

Converting the Second-Order Virial Coefficient, A_2, into the DPD Repulsive Magnitude, A. The experimental observations indicate that repulsive interactions between aggregates decrease with primary particle size. An increase in the degree of primary particle aggregation, z, with $S/V = 6/(d_p)$ suggests stronger short-range attractive interactions with smaller primary particle size. Potential functions with short-range attraction of primary particles and long-range repulsion of clusters have been shown to lead to stable dispersions of nanoparticle clusters.[44,45] In this case, as primary particles approach at short distances, the solvent and surfactant molecules may be excluded, allowing van der Waals interactions between the pigment particles.[46] For very large primary particles, there is insufficient specific surface area to bind the primary particles and the degree of aggregation will be low. A critical size scale can be determined from the intercept at $z = 1$ of about 60 nm (Figure 5). A similar critical size is observed in Figure 4, based on A_2, indicating a transition from attractive to repulsive long-range interactions at primary particle sizes of about 68 nm. van Rijssel et al. observed parallel behavior for quantum dot nanoparticles using a square-well attractive interaction potential for the clustering of primary particles.[47]

The values of A_2 were converted to a "per-aggregate" basis, $B_2 = A_2M^2/N_A$, to translate the small-angle scattering results into magnitudes of the repulsive force used in DPD simulations, "A". The molar mass is calculated by $M = \pi z \rho d_p^3/6$ using a spherical approximation. The relationship between the experimental B_2 and the DPD repulsive magnitude, A, is plotted in Figure 7 using eqs 6 and 7. Along each curve, one can read the value of A which yields a second virial coefficient similar to the experimental value; these points are shown for each PY14 sample series. Although there is a clear trend in A_2 versus d_p (plotted in Figure 4), there is no such trend in B_2 versus d_p, as shown in Figure 7, because B_2 has been normalized to an aggregate basis. Because the relationship between B_2 and A in DPD simulations is governed solely by the size of the dispersed aggregate, this general approach is applicable to a wide range of systems containing nanoparticulate fractal aggregates such as a rubber filled with fumed silica and carbon black.[42] Coupling small-angle scattering results to coarse-grain simulation parameters enables a predictive approach to determine the optimal conditions for dispersions of nanoparticulate aggregates.

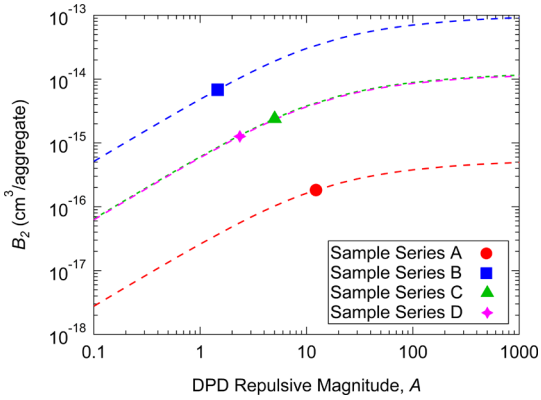

Figure 7. Calculated second-order virial coefficient per aggregate vs amplitude of DPD repulsive force using Eqs 6 and 7. Dashed lines show the trend in B_2 with A for a given aggregate size, R_{eted}, and points indicate the value of A which yields the experimental B_2 shown in Table 2.

CONCLUSIONS

Complex structures can emerge when aggregated nanoparticles enter the semidilute regime such as in the drying of inks and paint containing organic pigments. The emergence of structure

DOI: 10.1021/acs.langmuir.7b03033
Langmuir 2017, 33, 14029−14037

under semidilute conditions is related to the structure of the dilute aggregates and the interaction potential between aggregates. Kinetic simulations could predict such emergence using these input parameters. The organic pigment PY14 was studied as an example of the importance of emergent structure to predict properties such as brilliance and opacity. In this pigment, an aggregate network is formed which is defined by the percolation threshold and network mesh size. The emergence of the aggregate network is governed by a short-range, attractive potential that encourages aggregation and results in the degree of aggregation, z, as well as by long-range, repulsive interactions that ensure dispersion of aggregates. The mesh size emerges from the impact of long-range repulsive interactions as reflected by A_2 or ν, on the aggregate structure reflected by z and d_p. A_2 can be translated into a simple potential by integration. Such potential functions can be used to predict emergence of the filler network and other structures in more complex situations at higher concentrations through coarse-grain simulations.

The strength of binary interactions characterizing aqueous dispersions of PY14 can be determined using the second-order virial coefficient. Through USAXS measurements, the nanostructure of pigment dispersions may be characterized across multiple hierarchical structural levels for each pigment concentration series. Mass fractal aggregates of the smallest primary particle size exhibited the highest degree of aggregation, z, fractal dimension, and branch fraction as well as the highest value of A_2. The large value of A_2 suggests that these dispersions are the most stable. Large values of z indicate large short-range attractions that are linear in the specific surface area of the primary particles. The second virial coefficient was converted into the magnitude of repulsive interactions for use in coarse-grain simulations. These simulations may enable a predictive approach to control structural emergence in nanoscale dispersions and nanocomposites.

■ ASSOCIATED CONTENT

Supporting Information

The Supporting Information is available free of charge on the ACS Publications website at DOI: 10.1021/acs.langmuir.7b03033.

Fits to series A samples at 1 and 10%, plots of the USAXS data and the SAXS data, and a table of the functions used for calculations (PDF)

■ AUTHOR INFORMATION

Corresponding Author

*E-mail: gbeaucage@gmail.com.

ORCID

Gregory Beaucage: 0000-0002-6632-0889

Karsten Vogtt: 0000-0003-3206-1070

Notes

The authors declare no competing financial interest.

■ ACKNOWLEDGMENTS

A.M. was supported, in part, by the Department of Energy through the DOE Office of Science Graduate Student Research Program. Use of the APS, an Office of Science User Facility operated for the U.S. Department of Energy (DOE) Office of Science by Argonne National Laboratory, was supported by the U.S. DOE under contract no. DE-AC02-06CH11357. The USAXS data were collected at the APS on the beamline 9-ID-C operated by the X-ray Science Division. We gratefully acknowledge the vital assistance of Jan Ilavsky and his staff at 9-ID-C. This work was supported by the National Science Foundation through grants CMMI-1635865 and CMMI-1636036.

■ REFERENCES

(1) Skillas, G.; Agashe, N.; Kohls, D. J.; Ilavsky, J.; Jemian, P.; Clapp, L.; Schwartz, R. J.; Beaucage, G. Relation of the Fractal Structure of Organic Pigments to Their Performance. *J. Appl. Phys.* **2002**, *91*, 6120−6124.

(2) Mather, R. The Degree of Crystal Aggregation in Organic Pigments. *Dyes Pigm.* **1999**, *42*, 103−106.

(3) Faulkner, E.; Schwartz, R. *High Performance Pigments*; Wiley-VCH Verlag GmbH & Co. KGaA: Weinheim, Germany, 2009.

(4) Beaucage, G. Approximations Leading to a Unified Exponential/Power-Law Approach to Small-Angle Scattering. *J. Appl. Crystallogr.* **1995**, *28*, 717−728.

(5) Beaucage, G. Small-Angle Scattering from Polymeric Mass Fractals of Arbitrary Mass-Fractal Dimension. *J. Appl. Crystallogr.* **1996**, *29*, 134−146.

(6) Schaefer, D. W.; Martin, J. E.; Wiltzius, P.; Cannell, D. S. Fractal Geometry of Colloidal Aggregates. *Phys. Rev. Lett.* **1984**, *52*, 2371−2374.

(7) Kawamura, A.; Kohri, M.; Yoshioka, S.; Taniguchi, T.; Kishikawa, K. Structural Color Tuning: Mixing Melanin-Like Particles with Different Diameters to Create Neutral Colors. *Langmuir* **2017**, *33*, 3824−3830.

(8) Pratsinis, S. Flame Aerosol Synthesis of Ceramic Powders. *Prog. Energy Combust. Sci.* **1998**, *24*, 197−219.

(9) Schaefer, D. W.; Hurd, A. J. Growth and Structure of Combustion Aerosols: Fumed Silica. *Aerosol Sci. Technol.* **1990**, *12*, 876−890.

(10) Schaefer, D. W.; Olivier, B. J.; Hurd, A. J.; Beaucage, G. B. Structure of Combustion Aerosols. *J. Aerosol Sci.* **1991**, *22*, S447−S450.

(11) Beaucage, G.; Kammler, H. K.; Pratsinis, S. E. Particle Size Distributions from Small-Angle Scattering Using Global Scattering Functions. *J. Appl. Crystallogr.* **2004**, *37*, 523−535.

(12) Beaucage, G. Determination of Branch Fraction and Minimum Dimension of Mass-Fractal Aggregates. *Phys. Rev. E: Stat., Nonlinear, Soft Matter Phys.* **2004**, *70*, 1−10.

(13) Rai, D. K.; Beaucage, G.; Jonah, E. O.; Britton, D. T.; Sukumaran, S.; Chopra, S.; Gonfa, G.; Härting, M. Quantitative Investigations of Aggregate Systems. *J. Chem. Phys.* **2012**, *137*, 044311.

(14) Ramachandran, R.; Beaucage, G.; Kulkarni, A. S.; McFaddin, D.; Merrick-Mack, J.; Galiatsatos, V. Branch Content of Metallocene Polyethylene. *Macromolecules* **2009**, *42*, 4746−4750.

(15) Mulderig, A.; Beaucage, G.; Vogtt, K.; Jiang, H.; Kuppa, V. Quantification of Branching in Fumed Silica. *J. Aerosol Sci.* **2017**, *109*, 28−37.

(16) Sorensen, C. M. Light Scattering by Fractal Aggregates: A Review. *Aerosol Sci. Technol.* **2001**, *35*, 648−687.

(17) Strobl, G. *The Physics of Polymers*; Springer Berlin Heidelberg: Berlin, Heidelberg, 2007.

(18) Pedersen, J. S.; Sommer, C. Temperature Dependence of the Virial Coefficients and the Chi Parameter in Semi-Dilute Solutions of PEG. *Scattering Methods and the Properties of Polymer Materials*; Progress in Colloid and Polymer Science; Springer, 2005; Vol. *130*, pp 70−78.

(19) Bonneté, F.; Finet, S.; Tardieu, A. Second Virial Coefficient: Variations with Lysozyme Crystallization Conditions. *J. Cryst. Growth* **1999**, *196*, 403−414.

(20) Ho, J. G. S.; Middelberg, A. P. J.; Ramage, P.; Kocher, H. P. The Likelihood of Aggregation during Protein Renaturation Can Be

Assessed Using the Second Virial Coefficient. *Protein Sci.* **2003**, *12*, 708−716.
(21) Bymaster, A.; Jain, S.; Chapman, W. G. Microstructure and Depletion Forces in Polymer-Colloid Mixtures from an Interfacial Statistical Associating Fluid Theory. *J. Chem. Phys.* **2008**, *128*, 164910.
(22) Patel, N.; Egorov, S. Interactions between Colloidal Particles in Polymer Solutions: A Density Functional Theory Study. *J. Chem. Phys.* **2004**, *121*, 4987−4997.
(23) Vogtt, K.; Beaucage, G.; Weaver, M.; Jiang, H. Thermodynamic Stability of Worm-like Micelles. *Soft Matter* **2017**, *13*, 6068.
(24) Quigley, A.; Williams, D. R. The Second Virial Coefficient as a Predictor of Protein Aggregation Propensity: A Self-Interaction Chromatography Study. *Eur. J. Pharm. Biopharm.* **2015**, *96*, 282−290.
(25) Flory, P. J. *Principles of Polymer Chemistry*; Cornell University Press: Ithaca, NY, 1953.
(26) Striolo, A.; Ward, J.; Prausnitz, J. M.; Parak, W. J.; Zanchet, D.; Gerion, D.; Milliron, D.; Alivisatos, A. P. Molecular Weight, Osmotic Second Virial Coefficient, and Extinction Coefficient of Colloidal CdSe Nanocrystals. *J. Phys. Chem. B* **2002**, *106*, 5500−5505.
(27) Ilavsky, J.; Jemian, P. R. Irena: Tool Suite for Modeling and Analysis of Small Angle Scattering. *J. Appl. Crystallogr.* **2009**, *42*, 347−353.
(28) Glatter, O.; Kratky, O. *Small Angle X-ray Scattering*; Academic Press: New York, 1982.
(29) Tardieu, A.; Le Verge, A.; Malfois, M.; Bonneté, F.; Finet, S.; Riès-Kautt, M.; Belloni, L. Proteins in Solution: From X-Ray Scattering Intensities to Interaction Potentials. *J. Cryst. Growth* **1999**, *196*, 193−203.
(30) de Gennes, P. *Scaling Concepts in Polymer Physics*; Cornell University Press: Ithaca, 1979.
(31) North, S. M.; Jones, E. R.; Smith, G. N.; Mykhaylyk, O. O.; Annable, T.; Armes, S. P. Adsorption of Small Cationic Nanoparticles onto Large Anionic Particles from Aqueous Solution: A Model System for Understanding Pigment Dispersion and the Problem of Effective Particle Density. *Langmuir* **2017**, *33*, 1275−1284.
(32) Studart, A. R.; Amstad, E.; Gauckler, L. J. Colloidal Stabilization of Nanoparticles in Concentrated Suspensions. *Langmuir* **2007**, *23*, 1081−1090.
(33) Balasubramanian, R.; Kim, B.; Tripp, S. L.; Wang, X.; Lieberman, M.; Wei, A. Dispersion and Stability Studies of Resorcinarene-Encapsulated Gold Nanoparticles. *Langmuir* **2002**, *18*, 3676−3681.
(34) Groot, R.; Warren, P. Dissipative Particle Dynamics: Bridging the Gap between Atomistic and Mesoscopic Simulation. *J. Chem. Phys.* **1997**, *107*, 4423.
(35) Dzwinel, W.; Yuen, D.; Boryczko, K. Mesoscopic Dynamics of Colloids Simulated with Dissipative Particle Dynamics and Fluid Particle Model. *J. Mol. Model.* **2002**, *8*, 33−43.
(36) Liu, M.; Meakin, P.; Huang, H. Dissipative Particle Dynamics with Attractive and Repulsive Particle-Particle Interactions. *Phys. Fluids* **2006**, *18*, 017101.
(37) Liu, J.; Gao, Y.; Cao, D.; Zhang, L.; Guo, Z. Nanoparticle Dispersion and Aggregation in Polymer Nanocomposites: Insights from Molecular Dynamics Simulation. *Langmuir* **2011**, *27*, 7926−7933.
(38) Narayanan, J.; Liu, X. Y. Protein Interactions in Undersaturated and Superstaturated Solutions: A Study Using Light and X-ray Scattering. *Biophys. J.* **2003**, *84*, 523−532.
(39) Dong, J.; Chen, S.; Corti, D. S.; Franses, E. I.; Zhao, Y.; Ng, H. T.; Hanson, E. Effect of Triton X-100 on the Stability of Aqueous Dispersions of Copper Phthalocyanine Pigment Nanoparticles. *J. Colloid Interface Sci.* **2011**, *362*, 33−41.
(40) Ilavsky, J.; Jemian, P. R.; Allen, A. J.; Zhang, F.; Levine, L. E.; Long, G. G. Ultra-Small-Angle X-Ray Scattering at the Advanced Photon Source. *J. Appl. Crystallogr.* **2009**, *42*, 469−479.
(41) Ilavsky, J.; Zhang, F.; Allen, A. J.; Levine, L. E.; Jemian, P. R.; Long, G. G. Ultra-Small-Angle X-Ray Scattering Instrument at the Advanced Photon Source: History, Recent Development, and Current Status. *Metall. Mater. Trans. A* **2013**, *44*, 68−76.
(42) Jin, Y.; Beaucage, G.; Vogtt, K.; Jiang, H.; Kuppa, V.; Kim, J.; Ilavsky, J.; Rackaitis, M. A Pseudo-Thermodynamic Description of Compatibility for Binary Elastomer-Filler Blends. *Polymer* **2017**, *129*, 32−43.
(43) Vogtt, K.; Beaucage, G.; Weaver, M.; Jiang, H. Scattering Function for Branched Wormlike Chains. *Langmuir* **2015**, *31*, 8228−8234.
(44) Mossa, S.; Sciortino, F.; Tartaglia, P.; Zaccarelli, E. Ground-State Clusters for Short-Range Attractive and Long-Range Repulsive Potentials. *Langmuir* **2004**, *20*, 10756−10763.
(45) Bollinger, J. A.; Truskett, T. M. Fluids with Competing Interactions. II. Validating a Free Energy Model for Equilibrium Cluster Size. *J. Chem. Phys.* **2016**, *145*, 064903.
(46) Israelachvili, J. *Intermolecular and Surface Forces*, 3rd ed.; Academic Press: San Diego, 2011.
(47) van Rijssel, J.; Peters, V. F. D.; Meeldijk, J. D.; Kortschot, R. J.; van Dijk-Moes, R. J. A.; Petukhov, A. V.; Erné, B. H.; Philipse, A. P. Size-Dependent Second Virial Coefficients of Quantum Dots from Quantitative Cryogenic Electron Microscopy. *J. Phys. Chem. B* **2014**, *118*, 11000−11005.

DOI: 10.1021/acs.langmuir.7b03033
Langmuir 2017, 33, 14029−14037